Effect of Terrain on Path Loss in Urban Environments for Wireless Applications

Leonard Piazzi and Henry L. Bertoni, *Fellow, IEEE*

***Abstract*—Path-loss prediction algorithms for advanced wireless communication system planning have long considered the effect of electromagnetic propagation over buildings between the base station and subscriber. This phenomena is particularly important in residential areas, where the houses are typically a few stories high. For the most part, the buildings were assumed to lie on level terrain, although shadowing effects by terrain in the absence of buildings has been included. Previous works have offered a number of methods to quantitatively determine these effects from path profiles. This study examines propagation over buildings when the buildings are located on terrain features (hills). The buildings, which are represented by a series of absorbing half screens, are assumed to lie in rows that are equally spaced along parallel streets, with the streets running perpendicular to the terrain slope. Numerical results are obtained using successive repetition of the Kirchhoff–Huygens approximation. A phenomenological model based on ray optics for diffraction over a smooth surface is proposed as a way to interpret the numerical results. The dependence of model coefficients on terrain parameters are obtained from the numerical results.**

***Index Terms*—Propagation, terrain factors, urban areas.**

I. Introduction

CITIES are frequently built on undulating terrain or on rolling hills so that radio propagation may be simultaneously affected by both buildings and terrain. Based on measurements taken in Japan using very high base-station antennas, Okumura [1] accounted for terrain variability in a statistical sense through the use of a field strength correction factor and increased variability. However, this approach does not allow for the evaluation of the signal at specific locations even when the terrain is known. For portions of the terrain that are not shadowed, Lee [2] introduced the concept of effective antenna height to account for the actual terrain variation. When lower base-station antennas are used, even undulating hills may give rise to terrain blockage in some locations. While shadowing by hills in the absence of buildings has been studied [3]–[6], the combined effects of buildings and terrain does not appear to have been treated in the literature. In this study, we consider propagation over buildings on various terrain profiles in order to estimate the signal variability that terrain can introduce.

Away from the high-rise core of the city, base-station antennas for mobile radios are typically above or near to the rooftops of the surrounding buildings. In this case, propagation is thought to take place over the buildings and for flat terrain has been modeled by multiple forward diffraction past rows of buildings [7]–[11]. These models represent each row of buildings as an absorbing knife edge and via analytic or numerical techniques determine the loss associated with multiple forward diffraction over the knife edges. In order to model the path loss for the case of buildings on rolling hills, we assume the streets and, hence, the rows of buildings are oriented perpendicular to the plane of curvature of the hills, as shown in side view in Fig. 1, which is also assumed to be the plane of propagation. For mobiles located on the up slope of hills visible to the base station, as indicated by position ① in Fig. 1, the path loss can be found using the theory previously derived for flat terrain if the angle of incidence on the rooftops α in that theory is replaced by the angle α_1 to the local tangent plane, as indicated in Fig. 1. This method is equivalent to using an effective antenna height, as discussed by Lee [2]. However, these results do not apply when terrain shadowing occurs, such as at locations ② and ③ in Fig. 1.

Shadowing by hills in the absence of buildings has been modeled using absorbing knife edges [3] or dielectric wedges [4], as shown in Fig. 2 or circular cylinders [5], [6], as shown in Fig. 3. When an absorbing knife edge is used, the resultant path-loss predictions tend to be overly optimistic since important features of the terrain are omitted. The dielectric wedge formulation attempts to more accurately portray the physical properties of hills. Models utilizing diffraction over a circular cylinder further refine the problem and have yielded accurate results [5]. However, it is not clear how these methods apply when buildings are located on top of the hills. No matter the methodology, the results all indicate the importance of using a model that takes into account the effects of terrain blockage.

In this study, we assume the rows of buildings are of uniform height and spacing but are located on terrain with rolling hills, as suggested in Fig. 1. We first consider cylindrical and sinusoidal terrain variation. In order to treat the forward diffraction, each row of buildings is modeled as an absorbing knife edge. The field dependence above a knife edge is given as a function of the field above the previous knife edge and a direct numerical solution to the Kirchhoff–Huygens approximation is performed. Utilizing this method, over 100 knife edges may be considered with acceptable computation times. Fourier transform methods previously used to calculate multiple diffraction past screens of uniform height [12] have proven to be unworkable when there are large variations in the effective screen height (as needed in this study) and previously

Manuscript received August 27, 1997; revised January 12, 1998. The work of L. Piazzi was supported by a Motorola Partnership Research Grant.

The authors are with the Center for Advanced Technology in Telecommunications, Polytechnic University, Brooklyn, NY 11201 USA.

Publisher Item Identifier S 0018-926X(98)06096-7.

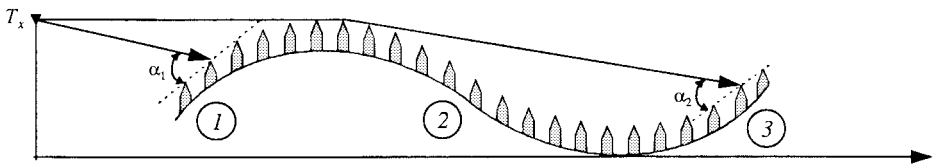

Fig. 1. Rows of houses on rolling terrain. For areas ① and ③ the angle with the local tangent may be used to determine the path loss.

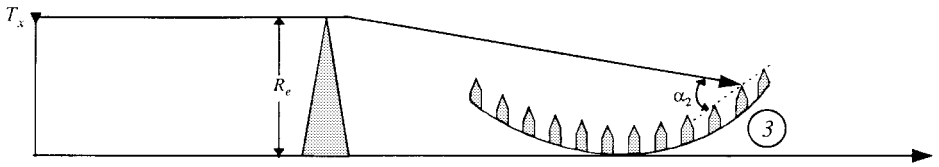

Fig. 2. Illustration of diffraction by an isolated hill that is represented by an equivalent knife edge or dielectric wedge.

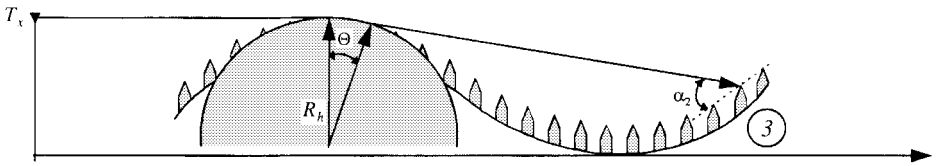

Fig. 3. Illustration of diffraction over a hill represented by a circular cylinder of radius R_h.

used analytic methods [10] are not applicable. The results we obtain indicate that a cylindrical representation for the hills in the terrain profile must be used, as opposed to single knife edge at the hill peak, or else the resultant path-loss values are too optimistic, particularly in the deep shadow of the hill.

The numerical techniques discussed above are too cumbersome to be incorporated into a cellular planning tool. We, therefore, interpret the numerical results in terms of ray optics in order to obtain a compact approximation. To make this interpretation, we make use of the ray formulation for diffraction over a smooth circular cylinder, which makes use of a creeping ray that travels on geodesic path around the cylinder. The field strength along the creeping ray decreases exponentially with arc length traveled on the surface of the cylinder with a decay factor that depends on the radius of the cylinder. Excitation of the creeping ray by a source is described by an excitation coefficient and subsequent radiation into space by a launch coefficient, which are also dependent upon the cylinder radius [13], [14]. It is interesting to note that although the numerical method assumed a nonsmooth surface over which the propagation occurs, the results are similar to those of a creeping wave solution for smooth cylinders.

In Section II, we develop the mathematical formalism used to numerically evaluate the Kirchhoff–Huygens integrals for forward diffraction past many absorbing half screens. Examples of the numerical results obtained for various hill geometries are discussed in Section III. The creeping ray formulation for propagation past a cylindrical hill is given in Section IV and is shown to accurately described the numerical results. Furthermore, fit equations are developed for the creeping ray attenuation and diffraction coefficients. In Section V, the creeping ray formulation is compared with the numerical integration results for the case of buildings on sinusoidal hills. Finally, in Section VI, we use the creeping ray formalism to develop path-loss formulas that can be compared with measurements or used by system designers.

II. Modeling Terrain Effects

Fig. 1 illustrates in cross-section rows of houses that are equally spaced along parallel streets, with the streets running perpendicular to the slope of the hills. In this example the transmitting antenna is placed at the maximum height of the terrain plus house height. For area ① in Fig. 1, the path loss may be determined using the Walfisch–Ikegami model, accounting for terrain slope by means of the local angle α_1. The path-loss ratio between isotropic antennas in watts received/watts transmitted is then given by

$$PL = \left(\frac{\lambda}{4\pi R}\right)^2 P_d[Q(\alpha_1)]^2. \tag{1}$$

The factor P_d is the diffraction loss from the last rooftop before the mobile down to the street and $Q(\alpha_1)$ is the multiple screen diffraction loss [10], which can be found from the polynomial approximation [15]

$$Q = 3.502g_p - 3.327g_p^2 + 0.962g_p^3 \tag{2}$$

over the range $0.01 < g_p < 1.00$, where the dimensionless parameter g_p is given by

$$g_p = \alpha\sqrt{\frac{d}{\lambda}} \tag{3}$$

where d is the separation between rows of buildings. For $g_p > 1.0$, the previous rows of buildings have almost no effect and $Q \approx 1.0$.

In region ③, to account for the blocking effect of the terrain between the subscriber and the transmitter, the path loss in

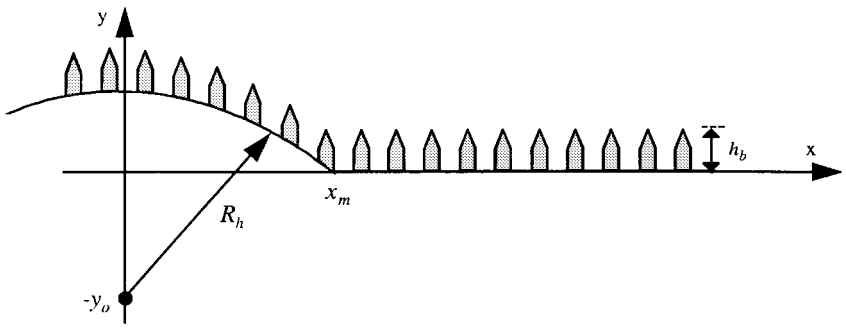

Fig. 4. Illustration of houses on an isolated cylindrical hill having radius of curvature R_h.

(1) must be multiplied by an appropriate loss factor P_D to account for the intervening hill loss. Fig. 2 shows one model, whereby the hill is replaced by an absorbing knife edge [3] or a dielectric wedge [4]. In the absence of buildings on top of the hill, the blockage may be modeled as a circular diffracting cylinder, as in Fig. 3, whose radius best fits the hill curvature [5], [6] in which case P_D is now the diffraction loss for the cylinder. The diffraction loss P_D, is typically a function of the cylinder radius R_h and θ, which is the angle determined by the two tangent lines to the cylinder—one from the transmitter and the other from the rooftop before the mobile [16]. The value of P_D when houses are present on the hills does not appear to have been previously considered. Similarly, the field reduction in region ② of Fig. 1 has not been previously considered and is even more complex than the other regions due to the curvature of the ground.

A. Isolated Cylindrical Hill

To facilitate the description of the field variation in regions ② and ③ of Fig. 1, we first characterize the terrain variation as that of an isolated cylindrical hill. To determine the effects of an isolated hill we make use of the terrain profile illustrated in Fig. 4. The height of the hill plus building height as a function of the distance x from the peak of the hill is given by

$$y = \sqrt{R_h^2 - x^2} - y_o + h_b \tag{4}$$

where R_h is the hill radius and $y_o > 0$ is the distance that the center of curvature lies below the flat portion of the terrain.

The maximum slope or *grade* of the hill occurs at x_m and is given by

$$\text{grade} = -\frac{dy}{dx} = \frac{x_m}{\sqrt{R_h^2 - x_m^2}}. \tag{5}$$

Knowing the grade and the horizontal distance x_m from the peak to the foot of the hill, (6) can be solved for the equivalent hill radius R_h

$$R_h = x_m\sqrt{1 + (1/\text{grade})^2}. \tag{6}$$

This expression is used to choose realistic values for R_h in carrying out the numerical evaluation discussed below. Examination of terrain elevation maps suggests that the radius of curvature of rolling terrain is typically much larger than 1 km.

B. Numerical Evaluation of the Line Source Fields

Since the Fresnel zones in the ultrahigh frequency (UHF) band out to a few kilometers are narrow, it is reasonable to use a two-dimensional (2-D) model by assuming the geometry in Fig. 4 to be uniform along z. Propagation oblique to the street grid can be accounted for by using the terrain profile and spacing d between rows of buildings as seen in the vertical plane containing the transmitter and receiver. On flat terrain this approach gives reasonable accuracy as compared to measurements for planes making angles as much as 60° to the street grid [17]. With the assumption of a 2-D model, the excess path loss due to the rows of buildings and terrain will be the same for a point source and for the fields radiated by a line source parallel to z. Propagation of the line source fields from the plane of one screen to the next is carried out numerically using the Kirchhoff–Huygens approximation. In this manner, we can account for diffraction past 100 or more screens and, therefore, can account for houses on sinusoidal and cylindrical terrain.

A uniform magnetic line source parallel to the z axis is located at the position of the transmitter (x_s, y_s) and radiates a cylindrical wave having only a z component of magnetic field $H(x, y)$, which, for $(kr \gg 1)$, is given by

$$H(x, y) \sim \frac{e^{jkr}}{\sqrt{kr}}. \tag{7}$$

This field is incident on the plane of the first knife edge. Subsequently, the electric field incident on the plane of the $n+1$ knife edge can be determined by the field above the nth knife edge using the approximate expression [18]

$$E(x_{n+1}, y_{n+1}) \approx ke^{-j\pi/4}\int_{h_n}^{\infty} E(x_n, y_n)\cos\theta_n \frac{e^{jkr}}{\sqrt{2\pi kr}}\, dy_n \tag{8}$$

where

$$\cos\theta_n = \frac{d}{r}$$
$$r = \sqrt{d^2 + (y_{n+1} - y_n)^2}. \tag{9}$$

Here, $d = x_{n+1} - x_n$ is the separation between successive rows of buildings. The lower limit h_n of the integration is equal to the height of the terrain at x_n plus the building height h_b. The numerical evaluation of (8) is carried out as in [7], where the integration is broken into discrete intervals over which

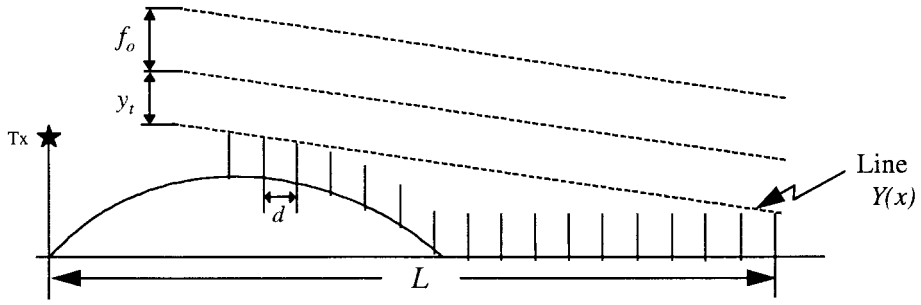

Fig. 5. Illustration of the truncation areas above the knife edges.

the amplitude and phase of the integrand are approximated by algebraic expressions that are integrated in closed form, thereby converting the integration into a summation. However, truncating the integration at a finite value of y does not follow the approach used in [7] since in that study the window function was tailored to the specific case of an incident plane wave field directed down toward the screens.

To terminate the summation above some height $Y(x)+y_t$ in the aperture of the knife edge, a window function is used that rolls off the field above $Y(x)+y_t$ to zero in a continuous fashion. For our case, the Kaiser–Bessel window function is used. It is given as follows:

$$W(y, h_n, y_t, f_o) = \begin{cases} 1, & h_n \le y < Y(x)+y_t \\ w(\xi), & Y(x)+y_t \le y < Y(x)+y_t+f_o \\ 0, & y \ge Y(x)+y_t+f_o \end{cases} \quad (10)$$

where

$$w(\xi) = 0.40208 + 0.49858\cos(\pi\xi) + 0.098\,11\cos(2\pi\xi) + 0.001\,23\cos(3\pi\xi) \quad (11)$$

with

$$\xi = \frac{y-(Y(x)+y_t)}{f_o}. \quad (12)$$

Here, $Y(x)$ is the straight line extending from the top of the building at the peak of the hill to the farthest building included in the calculation, as shown in Fig. 5. The integration aperture must be large enough to account for the area through which the fields propagate to the edge of the most distant screen. This aperture width is measured in terms of the Fresnel width for propagation from the source to the most distant edge. Thus, we take the termination point to lie outside the boundary of an ellipse drawn about a ray from the source to the $n+1$ screen. For accurately finding the fields in the shadow zone behind the hill, we have found it necessary to take the aperture to be six times the maximum half width of the Fresnel zone or

$$y_t = 3.0\sqrt{\lambda L}. \quad (13)$$

The field rolloff width f_o can be measured in terms of the Fresnel width for propagation from one edge to the next. To accurately find the fields in the shadow region, we have found it necessary to use

$$f_o = 15.0\sqrt{\lambda d}. \quad (14)$$

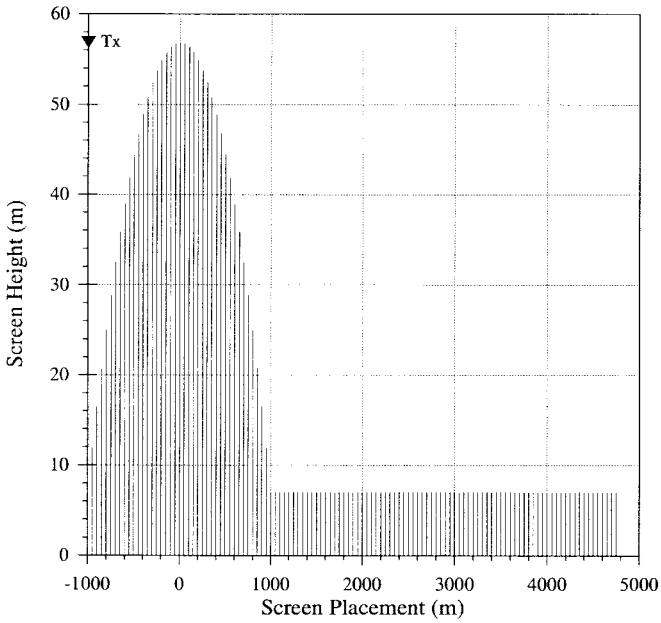

Fig. 6. Screen profile for typical hill radius parameters.

This choice of y_t and f_o are found to give stable computational results for the field at the top of successive half screens. When there is not a significant screen height variation, as in the case of flat terrain, the values of y_t and f_o maybe be reduced with no effect on the computational accuracy.

III. Numerical Results for a Cylindrical Hill

Numerical evaluation of the field due to a line source at the tops of successive rows of buildings (half-screens) were carried out for different horizontal separations d between the rows of buildings, different hill radii R_h, and different frequencies. The results for all cases are found to have similar characteristics that lead to a simple characterization. The half screens used to represent the rows of buildings for a typical case are shown in Fig. 6. The houses are 7 m high and the row separation d is 50 m. In this figure, the base of the hill occurs at $x_m = 1000$ m and the maximum grade is 10% so that the hill radius is 10.0 km and its maximum height is 50 m. The transmitting antenna is located at $x_s = -1000$ m and at a height y_s equal to the maximum screen height of 57 m.

The results of the numerical evaluation are shown in Fig. 7 for the screen profile given in Fig. 6. The field strength in decibels has a nearly linear variation on the back side of the hill

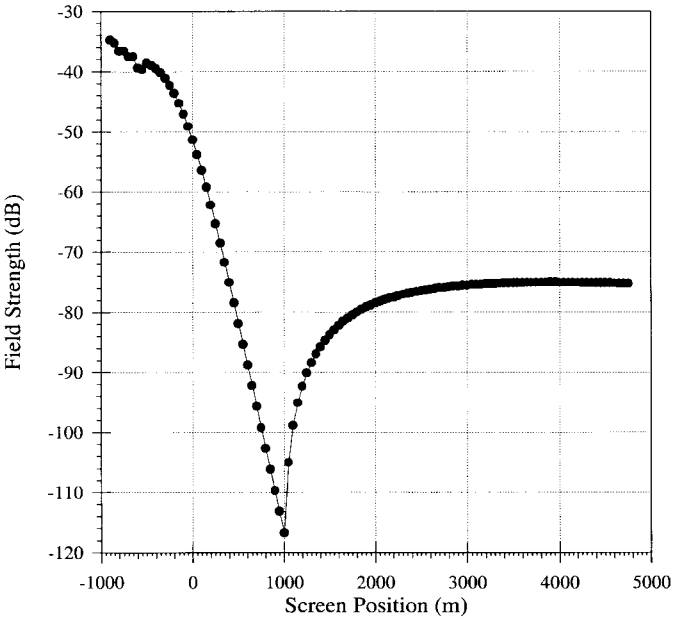

Fig. 7. Field strength versus screen position distance for the screen profile shown in Fig. 6.

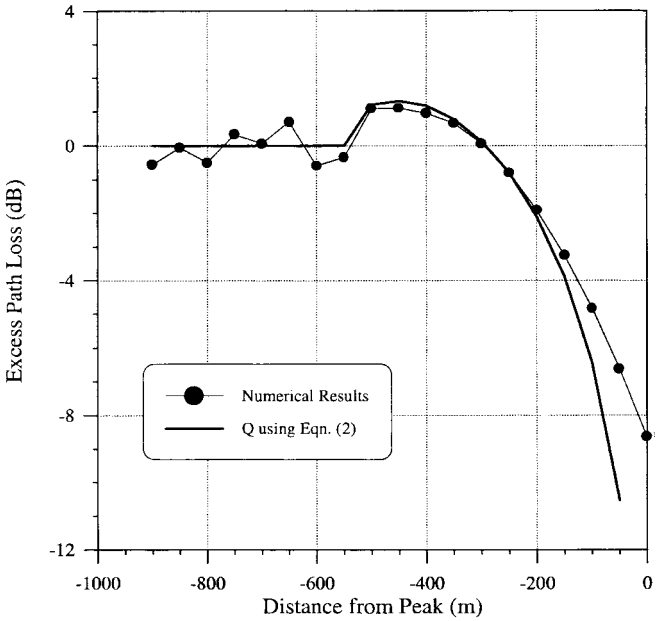

Fig. 8. Excess path loss on the front end of the hill in Fig. 6.

(0–1000 m), where diffraction from rooftop-to-rooftop occurs over a cylindrical-like surface. The minimum field strength value occurs at 1000 m, which is the base of the hill. After this point, the field strength increases out to about 3500 m, after which it decreases slowly. The same type of variation is found for all choices of hill radius R_h, row separation d and frequency, and can be modeled by a creeping wave.

The rise in field strength after the hill is attributable to the fact that the diffracted rays are now launched from points higher up on the hill and, thus, experience less diffraction loss before being launched. Immediately after the hill the foregoing effect more than compensates for the usual inverse distance dependence. However, for the rooftops far from the hill the rays are launched from near to the top of the hill so that the inverse distance dependence causes a decrease in signal strength.

Fig. 7 shows the results obtained by considering forward diffraction only and neglecting back diffraction from subsequent building rooftops. For buildings on flat terrain the back diffracted signal is smaller than that arriving from forward diffraction only. Because of the deep shadow at the base of the hill, as seen in Fig. 7, it may be possible for back diffraction from buildings on the flat terrain in Fig. 4 to fill in the shadow. In order to estimate the significance of back diffraction, we have evaluated the field at the base of the hill due to back diffraction from the next row of buildings. The uniform theory of diffraction (UTD) diffraction coefficient for a finite conductivity 90° wedge was used, thereby allowing for the observation point to lie in the transition region about the shadow boundary of the reflected wave. The back diffracted contribution was determined for various hill radii of interest and, assuming a 10% terrain slope at the base of the hill, was found to be approximately 16 dB less than the forward diffracted field at the base of the hill for all hill radii studied. Signals that are back diffracted from buildings further from the base of the hill must pass back over the buildings between the building in question and the base of the hill. Treating the back diffracting edge as a equivalent line source, it is found that the first row of buildings on the flat terrain gives the strongest back diffraction contribution. Therefore, we conclude that the back diffracted contributions are not significant for the cases considered.

A. Ray Optics for Rooftops Within LOS

We have compared the numerical integration results with the approximation (1) for those rooftops on the side of the hill facing the base station. Fig. 8 shows the path loss in excess of free-space loss obtained from the numerical results shown in Fig. 7 for $-900 < x_n < 0$. For comparison, we have also plotted $Q(\alpha_1)$ using the local terrain angle. It is seen that the ray method (1) is quite accurate up to the last few rooftops before the top of the hill at $x_n = 0$. Note that for $x_n < -500$, g_p given by (3) is greater than 1.0 and the approximation that there is no excess path loss ($Q = 1.0$) is used, which is consistent with the numerical results. As we approach the top of the hill α_1 approaches zero and using (2) proves to be overly pessimistic by approximately 4 dB.

IV. Creeping Rays for Non-LOS Rooftops

The creeping ray representation for the field diffracted by a circular cylinder is shown in Fig. 9 for points outside of the transition region centered on the shadow boundary. Unlike the case of diffracting from absorbing screens for which the TE and TM polarizations have the same path loss, in the case of a conducting cylinder the two polarizations behave differently.

The asymptotic representation for the creeping ray field at observation points behind the cylinder for an incident plane

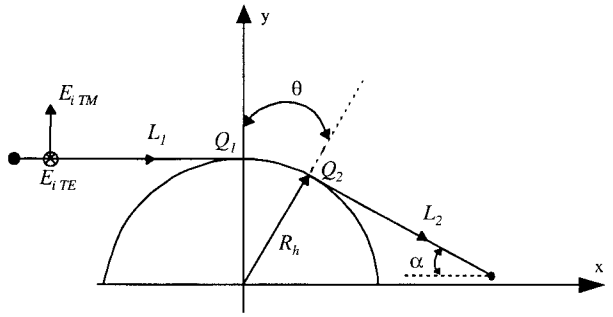

Fig. 9. Diffraction by a circular cylinder.

or cylindrical wave is [13]

$$E_{\mathrm{TM,\,TE}} \sim E_i(Q_1) e^{-jk\theta R_h} \frac{e^{-jkL_2}}{\sqrt{kL_2}} \cdot \sum_{p=1}^{\infty} D_p^{m,e}(R_h) \cdot \exp(-\psi_p^{m,e}\theta). \tag{15}$$

Here, $E_i(Q_1)$ is the incident field at the excitation point and L_2 is the distance from the launch point to the observation point. The attenuation constants ψ_p^m for TM polarization and ψ_p^e for TE polarization are given by

$$\psi_p^{m,e} = a_p^{m,e} \left(\frac{kR_h}{2.0}\right)^{1/3} e^{j\pi/6} \tag{16}$$

where the values of $a_p^{m,e}$ are found from the zeros of the Airey function $A_i(a_p)$ or its derivative. The first few terms for the TE polarization are $a_1^e = 2.338$, $a_2^e = 4.088$, and $a_3^e = 5.521$. The excitation coefficients are

$$D_p^{m,e} = C_p^{m,e} 2.0 \left(\frac{kR_h}{2.0}\right)^{1/3} e^{j\pi/6} \tag{17}$$

where the values of C_p for the TE polarization are functions of a_p^e and $A_i'(-a_p^e)$.

Note that the coefficients $D_p^{m,e}$ and $\Psi_p^{m,e}$ are functions of hill radius and frequency. Near the shadow boundary where θ is small, the sum is slowly convergent, while deeper into the shadow where the higher terms in the sum have decayed more rapidly, a good approximation is obtained by keeping only the $p = 1$ term. The values of ψ_p^m for TM polarization are smaller than those for TE polarization and for $p = 1$ it is smaller by the factor 2.3.

A. Ray Optics for the Backside of the Hill

For simplicity in representing the results obtained from the numerical integration, we retain only the first term in the creeping ray representation. To find the attenuation coefficient ψ, we examine the field at the top of the screens on the back side of the hill before the ray is launched. The field amplitude at these points due to a line source at a distance L_1 from the top of the hill is assumed to be of the form

$$|E(x_n, h_n)| = \frac{1}{\sqrt{kL_1}} D_H e^{-\psi\theta}. \tag{18}$$

The coefficients D_H and ψ are determined from the multiple integration results, as shown in Fig. 7, by fitting the numerical values at the farthest end of the hill. Because the values of x_n on the back side of the hill are much less than the hill radius, the angle $\theta \approx x_n/R_h$ so that (18) predicts a linear variation of the field in decibels, with x_n. In Fig. 7 the variation with x_n of the field strength in decibels, at the top of the screens (as obtained from the multiple integration) is seen to be nearly linear indicating the dominance of the $p = 1$ term in (15). The deviation from linearity reflects the importance near the shadow boundary of the terms in (15) having $p > 1$.

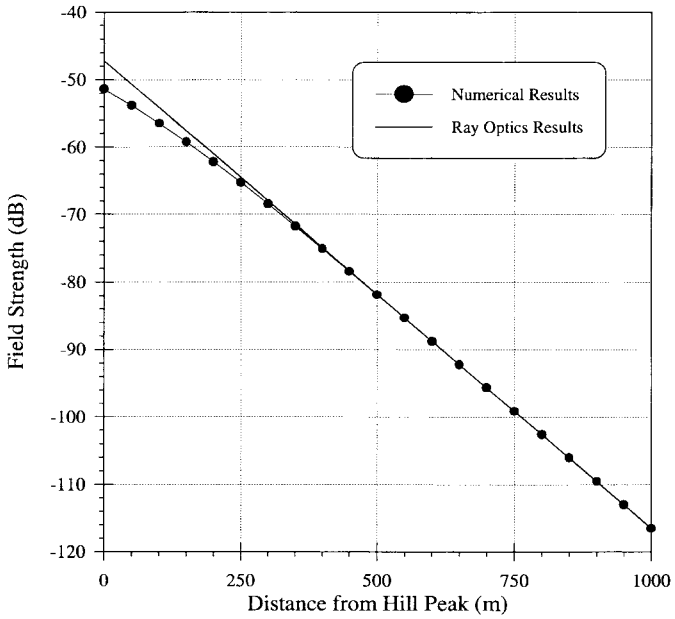

Fig. 10. Field strength predictions using the numerical and ray-optics approach on the back side of the hill in Fig. 6.

Fig. 10 shows a comparison of the field amplitude on the back side of the hill obtained from the approximation of (18) with the field computed by numerical integration. The location of the minimum field strength value (1000 m) is seen from (18) to result from the creeping ray that travels the greatest distance around the cylinder. As we approach the peak of the hill from the back side using the ray-optics method the result is more optimistic than the numerical integration result. Had more terms of the type shown in (15) been used to fit the computed results, a better fit would have been obtained close to the peak of the hill. It is also interesting to note that the results using (2), as we approach the peak from the front side are pessimistic rather than optimistic, as indicated in Fig. 10. Moreover, for the first rooftop on either side of the peak the magnitude of the error in decibels is similar.

The attenuation coefficient ψ is a function of hill radius R_h, frequency, and screen spacing d. We have plotted ψ from the numerical integration results in Fig. 11 for a frequency of 900 MHz and screen separations of 50 and 100 m. For comparison, the attenuation coefficient ψ_1 from (16) for diffraction of a TE wave by a smooth hill [14] labeled "James" is also shown. The values of ψ found by fitting the numerical results are seen to be displaced downward from ψ_1 for a smooth hill by an amount that is nearly independent of R_h, but varies approximately as

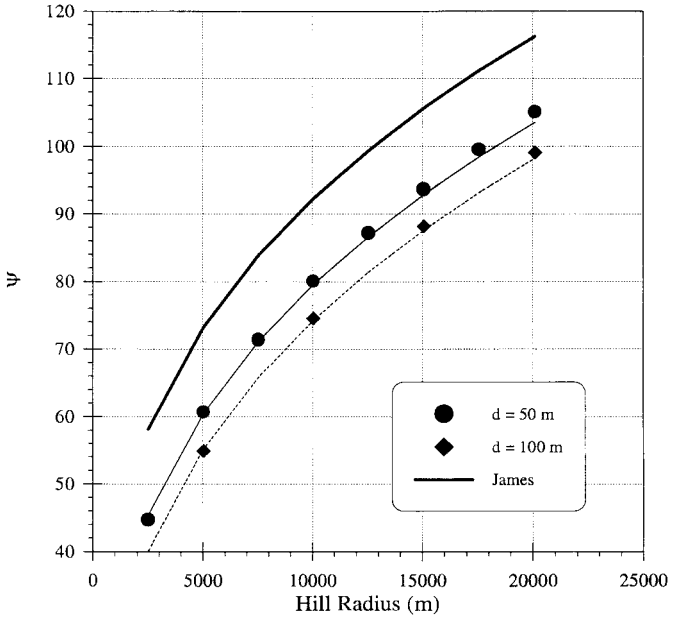

Fig. 11. Exponent loss factor ψ versus hill radius at 900 MHz computed for $d = 50, 100$ m and the theory for a smooth cylinder from James [14]. Approximate fit given by (19) is plotted as the continuous curves passing through the numerically computed points.

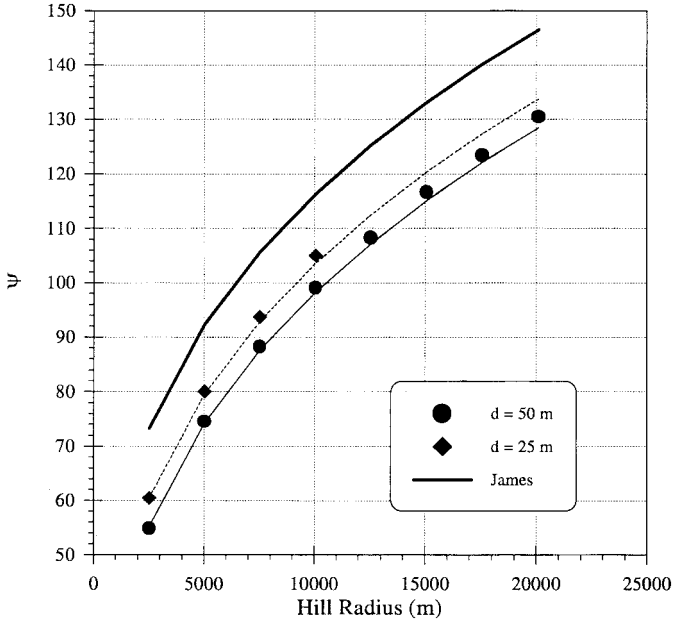

Fig. 12. Exponent loss factor ψ versus hill radius at 1800 MHz computed for $d = 25, 50$ m and the theory for a smooth cylinder from James [14]. Approximate fit given by (19) is plotted as the continuous curves passing through the numerically computed points.

$1.04\sqrt{d/\lambda}$. Thus, we find the simple approximation

$$\psi = 2.02\left(\frac{\pi R_h}{\lambda}\right)^{1/3} - 1.04\sqrt{\frac{d}{\lambda}} \tag{19}$$

which reduces to the theoretical diffraction result over a smooth hill for TE polarization [14] when $\sqrt{d/\lambda} = 0$. The variation of ψ predicted by (19) is indicated by the continuous curves in Fig. 11, which are seen to give a good fit to the values of ψ obtained from the numerical results.

Fig. 12 shows ψ versus hill radius for a frequency of 1800 MHz and for screen separations of 50 and 25 m. The values of ψ obtained from (19) are also indicated as continuous curves and are again seen to be accurate over the hill radii studied. The results in each case are consistent, noting from (16) that when the frequency is doubled ψ should increase by $2^{1/3} = 1.26$. Figs. 11 and 12 indicate that this trend is indeed the case, where the numerical results increase by an average factor of 1.24 or $2^{0.31}$ when the frequency is doubled.

The excitation coefficient D_H in (18) is found from the fit to the numerical results and is plotted in Fig. 13 versus hill radius for two values of frequency and screen separation d. The variation of D_H with the various parameters may be approximated by

$$\ln(D_H) = 3.75 + (-0.648 + 0.072\ln(d/\lambda))\ln(R_h/\lambda) - 0.259\ln(d/\lambda). \tag{20}$$

The values of D_H obtained from this expression are indicated by the continuous curves in Fig. 13.

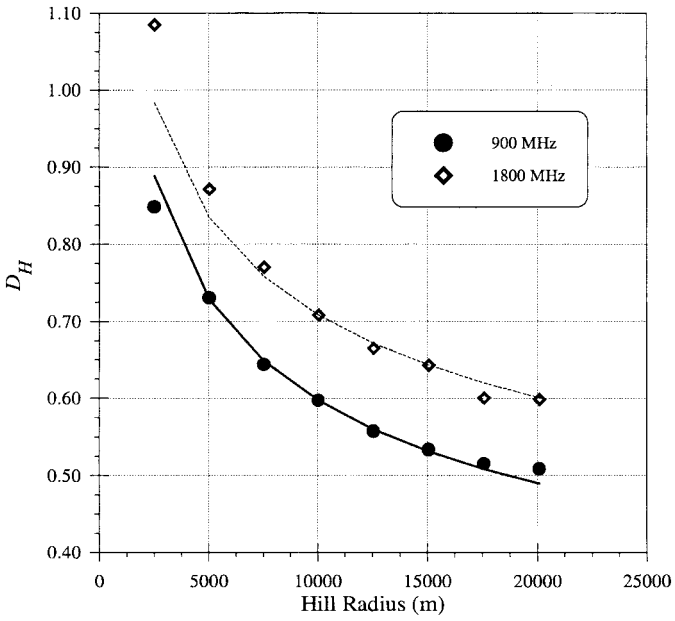

Fig. 13. Coefficient D_H giving the fields on the back of the hill for $d = 50$ m. Approximate fit given by (20) is plotted as the continuous curves passing through the numerically computed points.

B. Ray Optics After the Hill

To model the signal at the rooftops on the flat terrain following the hill in terms of creeping rays, we make use of (15) keeping only the first term for the fields above the flat terrain after the hill, as shown in Fig. 6. In order to separate the effect of diffraction over the hill from the effect of diffraction by the screens on the flat terrain following the hill, we have separately computed the field for the case when the only screens present are those on the hill, e.g., when the screens for distances greater than 1000 m in Fig. 6 have been removed. The numerical results for the field at the location of the edges of the screens that were removed are shown in Fig. 14 for the hill profile of Fig. 6, assuming a frequency of 900 MHz and a screen separation of 50 m.

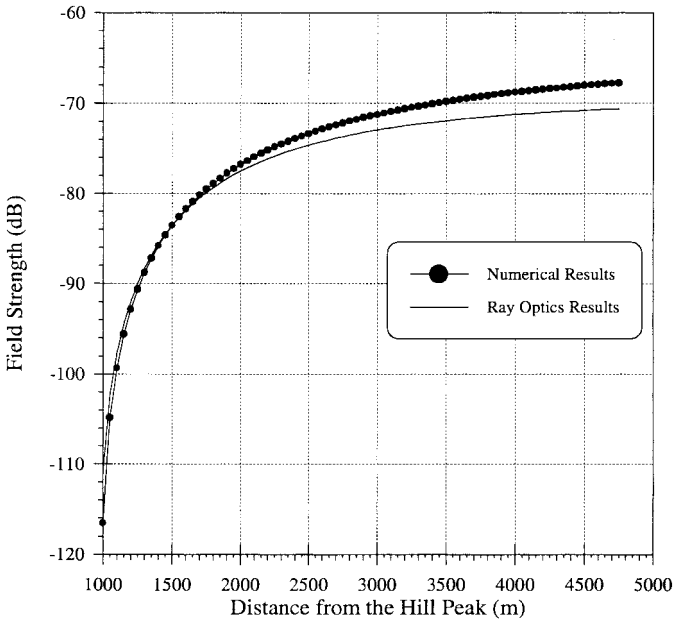

Fig. 14. Field-strength predictions using the numerical and ray-optics approach.

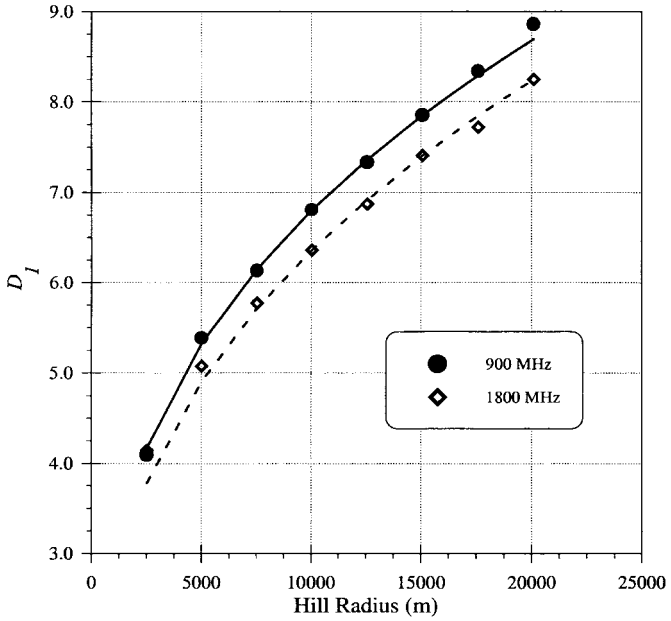

Fig. 15. Coefficient D_1 versus hill radius for $d = 50$ m. Approximate fit given by (21) is plotted as the continuous curves passing through the numerically computed points.

The ray-optical results obtained using the first term in (15) are also shown in Fig. 14. We have used the value of ψ taken from Fig. 11 and selected a value of D_1 to match the numerical results when the launch angle is fixed at 1.7°. Because this coefficient is determined by fitting the ray-optics solution to the numerical integration results at a point close to the base of the hill, the ray-optical predictions deviate by a few decibels from the numerical result at greater distances. It is believed that had more terms been included in (15), the results would more closely match.

Fig. 15 shows the variation of the ray-optics coefficient D_1 used in the creeping ray formulation with hill radius for different frequencies. The variation of D_1 with hill radius, screen separation, and wavelength can be approximated by the formula

$$\ln(D_1) = 2.22 + (0.19 + 0.031\ln(d/\lambda))\ln(R_h/\lambda) - 0.79\ln(d/\lambda). \quad (21)$$

This coefficient increases as R increases in a manner similar to that given in (17). However, the magnitude of the coefficients given in (17) are significantly larger than those given by (21).

In order to account for the presence of buildings on the flat terrain after the hill (as in Fig. 4), the ray-optics formulation of (15), which accounts for the multiple diffraction loss over the buildings on the hill, must be augmented by $Q(\alpha)$ in (2) to account for multiple diffraction past the buildings on the flat terrain. Using the angle α shown in Fig. 9, we have computed the field reaching the rooftops on the flat terrain and compared these results with those obtained from numerical integration. The field strength computed by these two methods for the geometry of Fig. 6 are plotted in Fig. 16. The results in Fig. 16 are consistent with the computations shown in Fig. 14, for the case when no buildings are present on the flat terrain. Again improvement is possible with the addition of more terms in (15). It is of interest to note that the differences between the numerical integration results in Fig. 16 and those in Fig. 14 are indeed approximately equal to $Q(\alpha)$ determined from (2).

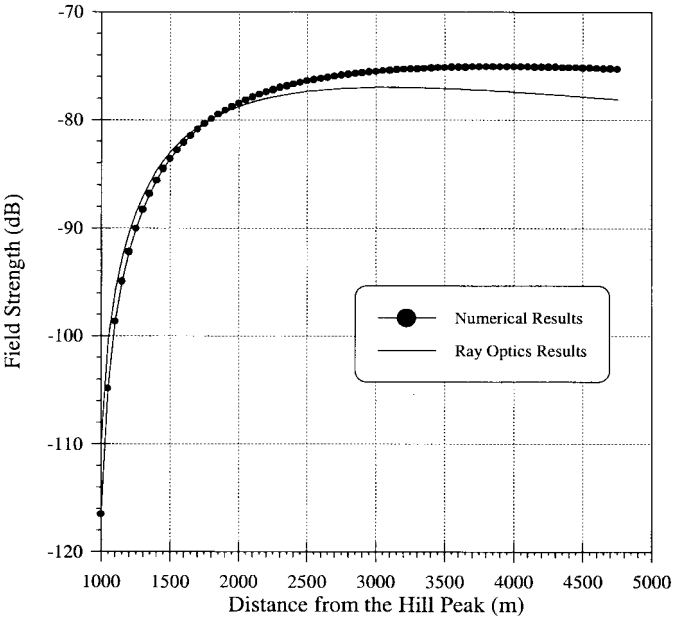

Fig. 16. Field strength predictions using the numerical and ray-optics approach with the screens present on the flat terrain after the hill.

V. Sinusoidal Hills—Shape Sensitivity

It is also interesting to examine the effects of house placement on a sinusoidal varying profile, not unlike Fig. 1. Fig. 17 illustrates the path profile for a sinusoidal varying terrain, where the cylinder of Fig. 6 approximately fits the first peak of Fig. 17. Fig. 18 shows the numerical results for this profile. An interesting phenomena to note is that the minimum field strength value does not correspond to the trough of the terrain

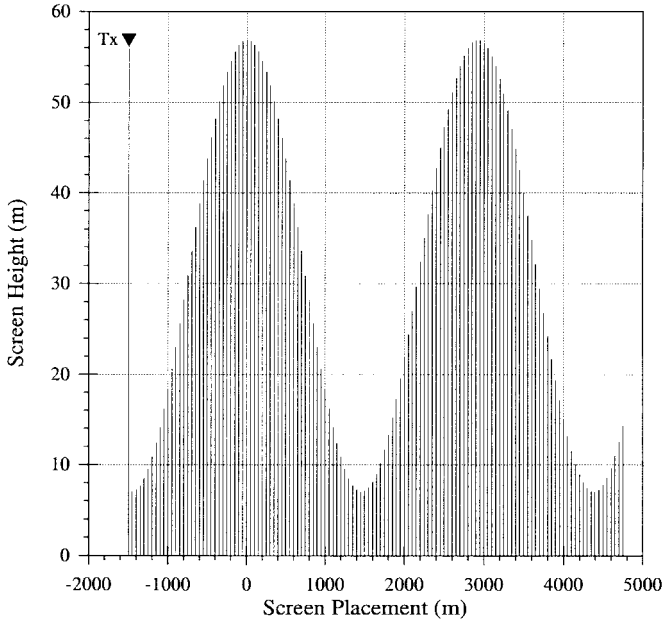

Fig. 17. Screen profile for a sinusoid-like terrain path.

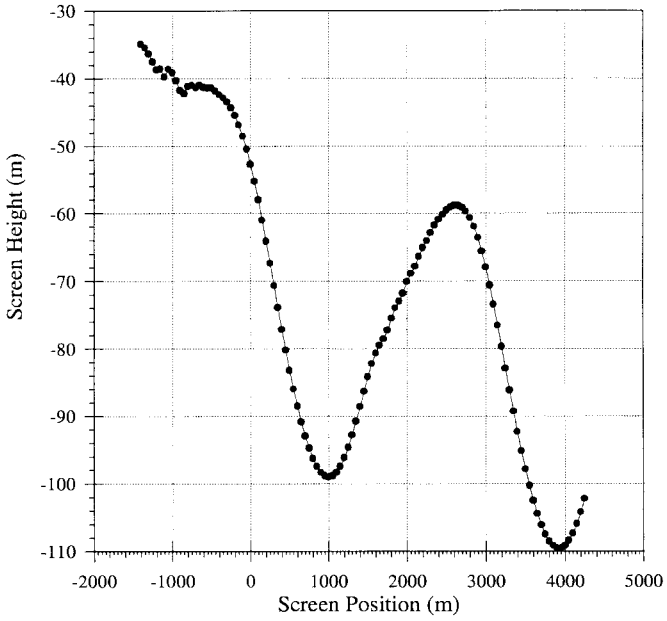

Fig. 18. Field-strength variation for a sinusoidal varying hill profile.

profile at 1500 m, but rather at the inflection point of the terrain preceding the trough. This behavior is consistent with the creeping ray interpretation since the field at the terrain minimum is due to a ray that is launched from a point further up the hill and, therefore, has experienced less exponential loss then at the inflection point. Also, the second maximum of the field strength does not correspond to second peak of the terrain profile, but rather occurs before this point as a result of diffraction by the previous screens. After the second peak, the field strength again decreases linearly, as was previously described.

Fig. 19 shows the ray optics and numerical solution for some of the screens between the first and second peaks

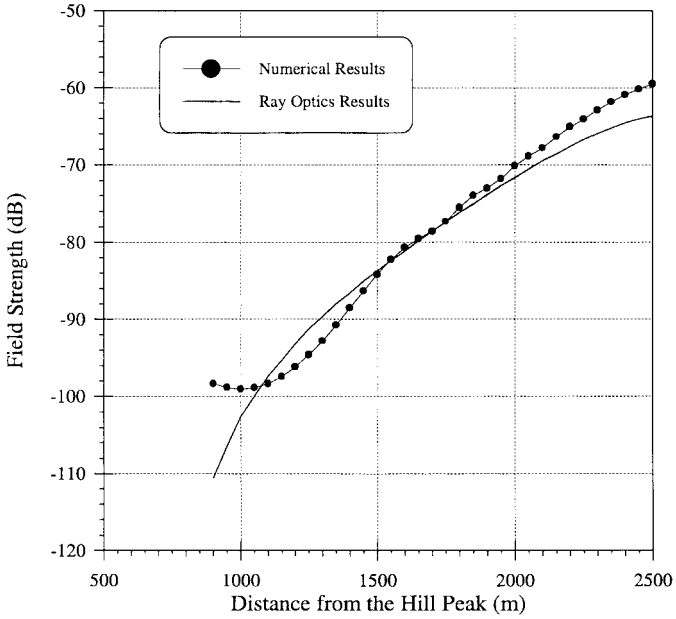

Fig. 19. Field-strength predictions using the numerical and ray-optics approach.

indicated in Fig. 17. In order to do this, we replace the first peak by a cylinder to determine the creeping ray loss and then use the local angle determined by the terrain to find $Q(\alpha)$. The result of using this method for screens near to the top of the second peak unfortunately is an overly pessimistic prediction for two reasons. First, the screens near the second peak are in the transition region about the shadow boundary from the first peak and, therefore, more terms are needed in (15) for more accurate results. Second, at the top of the hill the results from (2) are unusable because α approaches zero. The results match closely on the second slope, but the ray-optics predictions are pessimistic near the trough where the approximation for $Q(\alpha)$ is again inaccurate due to the small local angle. However, the creeping ray approximation is sufficiently accurate for wireless system planning at locations on the up slope of the shadowed hill.

VI. Path Loss Between Isotropic Antennas

For the mobile-system design engineer, the efficient evaluation of path loss between isotropic antennas is of particular interest. In this regard, we generalize the previous results for a line source by accounting for spreading of rays in the direction perpendicular to the plane of incidence. At points on the shadowed side of a hill such as location ② in Fig. 1, the path-loss ratio between received and transmitted power is

$$P_L = \left(\frac{\lambda}{4\pi}\right)^2 \frac{e^{-2\psi\theta}}{RL_1} D_H^2 P_d. \tag{22}$$

Assuming that vertical displacements are small compared to the horizontal displacements, R is the distance from the base station to the mobile. Also, L_1 is the distance from the base station to the hill along a ray that is just tangent to the hill. The diffraction loss down to the mobile from the preceding building is given by P_d, and D_H and ψ are given by (20) and (19) for the appropriate hill radius.

For locations such as ③ in Fig. 1 that are shadowed by a previous hill, the path-loss ratio is

$$P_L = \left(\frac{\lambda}{4\pi}\right)^2 \frac{e^{-2\psi\theta}}{RL_1L_2} D_1^2 Q^2(\alpha) P_d \tag{23}$$

where R is again the distance between the base station and the mobile. Also, L_1 is as previously defined and L_2 is the distance from the launch point on the hill to the building just before the mobile. Here $Q(\alpha)$ is the multiple diffraction loss due to the rows of houses before the mobile and D_1 is obtain from (21).

VII. Conclusions

This work has demonstrated that multiple diffraction past absorbing half screens on a cylindrical path profile can be parameterized as creeping ray behavior around a cylinder. Consistent with the ray-optics formulation, we have determined necessary coefficients as a function of frequency, hill radii, and screen separation. In the limit as the screen separation approaches zero, the exponential loss factor ψ approaches that of TE diffraction by a smooth cylinder. The diffraction coefficient D_1 is significantly smaller than that given by the smooth cylinder formulations. The effects of considering houses on the terrain profile is similar to adding a roughness factor to the diffraction results for a smooth cylinder; that is, for observations in the deep shadow, the path loss is greater when the houses are considered. This is consistent with the work in [19].

Using the fit equations given in this work the path loss over buildings located on rolling terrain may be determined. However, the results for sinusoidal hills show that the ray-optics approach must be improved to handle the transition region effects and the multiple diffraction effects at very small angles α.

References

[1] Y. Okumura, E. Ohmori, T. Kawano, and K. Fukuda, "Field strength and its variability in VHF and UHF land-mobile radio service," *Rev. Elect. Commun. Lab.*, vol. 16, no. 9/10, pp. 825–884, Sept./Oct. 1968.

[2] W. C. Y. Lee, "Studies of base-station antenna height effects on mobile radio," *IEEE Trans. Veh. Technol.*, vol. VT-29, pp. 252–260, May 1980.

[3] K. Bullington, "Radio propagation for vehicular communications," *IEEE Trans. Veh. Technol.*, vol. VT-26, pp. 295–308, Nov. 1977.

[4] G. Lampard and T. Vu-Dinh, "The effect of terrain on radio propagation in urban microcells," *IEEE Trans. Veh. Technol.*, vol. 42, pp. 314–317, Aug. 1993.

[5] D. E. Eliades, "Alternative derivation of the cascaded cylinder diffraction model," *Proc. Inst. Elect. Eng.*, vol. 140, no. 4, pp. 279–284, Aug. 1993.

[6] J. D. Parsons, *The Mobile Radio Propagation Channel*, 1st ed. New York: Wiley, 1992.

[7] J. Walfisch and H. L. Bertoni, "A theoretical model of UHF propagation in urban environments," *IEEE Trans. Antennas Propagat.*, vol. 36, pp. 1788–1796, Dec. 1988.

[8] H. H. Xia and H. L. Bertoni, "Diffraction of cylindrical and plane waves by an array of absorbing half screens," *IEEE Trans. Antennas Propagat.*, vol. 40, pp. 170–177, 1992.

[9] S. R. Saunders and F. R. Bonar, "Prediction of mobile radio wave propagation over buildings of irregular heights and spacings," *IEEE Trans. Antennas Propagat.*, vol. 42, pp. 137–144, Feb. 1994.

[10] L. R. Maciel, H. L. Bertoni, and H. H. Xia, "Unified approach to prediction of propagation over buildings for all ranges of base station antenna height," *IEEE Trans. Veh. Technol.*, vol. 42, pp. 41–45, Feb. 1993.

[11] L. E. Vogler, "An attenuation function for multiple knife-edge diffraction," *Radio Sci.* vol. 19, pp. 1541–1546, 1982.

[12] J.-E. Berg and H. Holmquist, "An FFT multiple half-screen diffraction model," in *Proc. Veh. Technol. Conf.*, Stockholm, Sweden, June 1994, pp. 195–199.

[13] J. B. Keller, "Diffraction by a convex cylinder," *IEEE Trans. Antennas Propagat.*, vol. AP-24, pp. 312–321, 1956.

[14] G. L. James, *Geometrical Theory of Diffraction for Electromagnetic Waves.* Stevenage, U.K.: Peter Peregrinus Ltd., 1976.

[15] H. L. Bertoni, W. Honcharenko, L. R. Maciel, and H. H. Xia, "UHF propagation prediction for wireless personal communications," *Proc. IEEE* vol. 82, no. 9, pp. 1333–1359, Sept. 1994.

[16] L. B. Felsen and N. Marcuvitz, *Radiation and Scattering of Waves.* Englewood Cliffs, NJ: Prentice-Hall, 1973.

[17] L. R. Maciel, H. L. Bertoni, and H. H. Xia, "Propagation over buildings for paths oblique to the street grid," in *Proc. Int. Symp. Personal Indoor Mobile Radio Commun.*, Boston, MA, Oct. 1992, pp. 75–79.

[18] M. Born and E. Wolf, *Principles of Optics.* New York: Pergamon, 1964.

[19] K. Hacking, "R.F. propagation over rounded hills," *Proc. Inst. Elect. Eng.* vol. 117, no. 3, pp. 499–511, Mar. 1970.

Leonard Piazzi was born in Hudson, NY, on August 29, 1971. He received the B.S., M.S., and Ph.D. degrees all in electrical engineering from the Polytechnic University, Brooklyn, NY, in 1993, 1995, and 1998, respectively.

During the summer of 1995, he worked as an Intern Engineer at the Motorola Communication Systems Research Laboratory, in Schaumburg, IL. His research interests are centered in electromagnetics, particularly in wave propagation and diffraction theory for propagation modeling in urban environments for wireless communication systems.

Henry L. Bertoni (M'67–SM'69–F'87) was born in Chicago, IL, on November 15, 1938. He received the B.S. degree in electrical engineering from Northwestern University, Evanston, IL, in 1960, and the M.S. (electrical engineering) and Ph.D. (electrophysics) degrees both from the Polytechnic Institute of Brooklyn (now Polytechnic University), in 1962 and 1967, respectively.

In 1967, he joined the faculty of the Polytechnic, becoming Head of the Electrical Engineering Department (1990–1995) and serving as Vice Provost of Graduate Studies (1995–1996). His research has dealt with theoretical aspects of wave phenomena in electromagnetics, ultrasonics, acoustics, and optics. He has authored or coauthored more than 100 journal and proceedings papers on these topics. From 1982 to 1983 he spent a sabbatical leave at the University College London, U.K., as a Guest Research Fellow of the Royal Society. During the summer of 1983, he held a Faculty Research Fellowship at USAF Rome Air Development Center, Hanscom AFB. His current research in electromagnetics deals with the theoretical prediction of UHF propagation characteristics in urban environments.

Dr. Bertoni was the first Chairman of the Technical Committee on Personal Communications of the IEEE Communications Society and was IEEE representative to and chairman of the Hoover Medal Board of Award. He has served on the ADCOM of the IEEE Ultrasonics, Ferroelectric, and Frequency Control Society and is also a member of the International Scientific Radio Union and the New York Academy of Science. The research he carried out at University College was the subject for which he was awarded the 1984 Best Paper Award of the IEEE Sonics and Ultrasonics Group. One of his papers on UHF propagation characteristics in urban environments received the 1993 Neal Shepherd Best Propagation Paper Award of the IEEE Vehicular Technology Society.